PCCP

ROYAL SOCIETY OF CHEMISTRY

PAPER

View Article Online
View Journal | View Issue

Cite this: *Phys. Chem. Chem. Phys.*, 2024, **26**, 13364

Development of Pd/In_2O_3 hybrid nanoclusters to optimize ethanol vapor sensing†

Bo Xie,[a] Jian Sun,[a] Aoxue Zhang,[a] Haoyu Qian,[a] Xibing Mao,[a] Yingzhu Li,[a] Wenjing Yan,[a] Changjiang Zhou,[a] Hui-Min Wen,[a] Shengjie Xia,[a] Min Han,[b] Paolo Milani[c] and Peng Mao *[bd]

Received 28th February 2024,
Accepted 10th April 2024

DOI: 10.1039/d4cp00868e

rsc.li/pccp

In this study, we successfully synthesize palladium-decorated indium trioxide (Pd/In_2O_3) hybrid nanoclusters (NCs) using an advanced dual-target cluster beam deposition (CBD) method, a significant stride in developing high-performance ethanol sensors. The prepared Pd/In_2O_3 hybrid NCs exhibit exceptional sensitivity, stability, and selectivity to low concentrations of ethanol vapor, with a maximum response value of 101.2 at an optimal operating temperature of 260 °C for 6 at% Pd loading. The dynamic response of the Pd/In_2O_3-based sensor shows an increase in response with increasing ethanol vapor concentrations within the range of 50 to 1000 ppm. The limit of detection is as low as 24 ppb. The sensor exhibits a high sensitivity of 28.24 $ppm^{-1/2}$, with response and recovery times of 2.7 and 4.4 seconds, respectively, for 100 ppm ethanol vapor. Additionally, the sensor demonstrates excellent repeatability and stability, with only a minor decrease in response observed over 30 days and notable selectivity for ethanol compared to other common volatile organic compounds. The study highlights the potential of Pd/In_2O_3 NCs as promising materials for ethanol gas sensors, leveraging the unique capabilities of CBD for controlled synthesis and the catalytic properties of Pd for enhanced gas-sensing performance.

Introduction

Ethanol, primarily recognized as a renewable fuel, now poses significant environmental concerns due to its volatile nature.[1–4] Being widely used in industries like pharmaceuticals and beverages, ethanol is also a common urban and industrial pollutant.[5] Detecting and monitoring its levels are crucial for public health and safety, especially considering its association with industrial growth.[6–9] Ethanol testing spans environmental monitoring,[10] industrial safety,[11] and law enforcement,[12] making the development of sensitive detection methods imperative.[13] In addressing the demand for sensitive detection methods, gas sensors have undergone significant evolution over the decades, resulting in a wide array of types based on different sensing materials and methods. These include catalytic combustion, electrochemical, thermally conductive, infrared absorption, paramagnetic, solid electrolyte, and metal oxide semiconductor sensors. Among these, metal oxide semiconductor (MOS) gas sensors stand out prominently. As solid-state resistive sensors, MOS sensors find extensive application in toxic and explosive gas alarms, air quality monitoring, indoor pollutant detection, and medical diagnostics through breath analysis. Their widespread adoption is attributed to their high sensitivity, cost-effectiveness, production flexibility, and compatibility with modern electronics.[14]

Currently, the predominant sensing materials for reducing gases like ethanol are n-type MOS, including SnO_2,[15] In_2O_3,[16] WO_3,[17] and ZnO.[1,2] Each material offers distinct sensing properties, chosen based on specific requirements for sensitivity, selectivity, and operational conditions. Among these MOS, In_2O_3 stands out for its high electron mobility and excellent stability, which contribute to its outstanding gas-sensing properties. It demonstrates promising detection potential among various sensing materials.[18] Consequently, enhancing the gas-sensing performance of In_2O_3-based gas sensors has become a focal point of interest for researchers worldwide. Loading or doping with noble metals represents a crucial approach to enhance the gas-sensing properties of MOS. This method operates based on two main mechanisms: electronic sensitization and chemical sensitization.[19]

[a] *College of Chemical Engineering, Zhejiang University of Technology, Zhejiang 310014, P. R. China*
[b] *National Laboratory of Solid-State Microstructures, College of Engineering and Applied Sciences, Nanjing University, Nanjing 210093, P. R. China. E-mail: pmao@nju.edu.cn*
[c] *CIMAINA and Department of Physics, Università degli Studi di Milano, via Celoria 16, I-20133, Milano, Italy*
[d] *State Key Laboratory of Fluid Power and Mechatronic Systems, Zhejiang University, Hangzhou, 310027, P. R. China*

† Electronic supplementary information (ESI) available. See DOI: https://doi.org/10.1039/d4cp00868e

Traditional wet chemical methods, such as electrostatic spinning,[20,21] sol-gel processes,[22] solution methods,[23,24] and hydrothermal process,[25] have been extensively utilized for preparing ethanol vapor sensing materials. These methods are favored for their simplicity, cost-effectiveness, and the ability to produce materials with a broad range of properties. However, they pose challenges in terms of reproducibility of material properties and compatibility with semiconductor processes. Despite their widespread use, traditional wet chemical methods have limitations regarding the uniformity and purity of the produced materials, leading to potential performance uncertainties in the sensors. Moreover, the strategy of noble metal loading or doping to enhance gas-sensing performance further complicates traditional wet chemical methods, rendering them more complex and unpredictable. The incorporation of noble metals introduces additional variables that may affect material properties and sensor performance, exacerbating issues of reproducibility and control. Additionally, some of these methods involve complex procedures and the use of hazardous chemicals, raising environmental and safety concerns. Consequently, there is a growing interest in alternative synthesis techniques that offer greater control, reproducibility, and environmental friendliness.

Fortunately, the generation of beams of nanoclusters (NCs) in the gas phase and their subsequent deposition in vacuum represent a new and attractive approach to the production of nanostructured functional materials and devices. Cluster beam deposition (CBD) has found widespread application in the preparation of light-emitting devices,[26] SERS chips,[27] heterogeneous catalysts,[28] and plasmonic devices.[29,30] CBD offers significant advantages over traditional methods by enabling the controlled synthesis of NCs with precise sizes and compositions, eliminating the need for solvents and associated effluents.[31–33] This capability results in reliable material properties, which are crucial for developing sensors with high sensitivity and selectivity. More importantly, CBD effectively addresses the challenges associated with traditional wet chemical methods, providing a more advanced and precise approach to material synthesis for sensors.[32,34–36] CBD excels at producing materials with high purity and controlled morphology, allowing the synthesis of NCs with tailored shapes and sizes,[37,38] essential for optimizing sensor performance. CBD is particularly suitable for constructing MOS-based gas-sensing materials modified with noble metals. In our previous research,[39] CBD was used to construct a Pd-loaded SnO_2 hydrogen sensing material, successfully achieving a wide range of hydrogen detection. This confirms the applicability of CBD for the precise construction of MOS-based gas-sensing materials.

This study presents the development of a high-performance ethanol sensor utilizing palladium/indium trioxide (Pd/In_2O_3) hybrid NCs fabricated *via* CBD. The key objective is to overcome the limitations of existing materials and methods by achieving a sensor with significantly enhanced sensitivity, stability, and selectivity for ethanol detection. Our approach involves a single-step deposition of In_2O_3 NPs directly onto interdigital electrodes (IDEs), followed by the strategic integration of Pd to modulate sensor performance. This methodology merges the controlled synthesis advantages of CBD with the inherent catalytic properties of Pd, aiming to achieve previously unattainable levels of sensitivity, long-term stability, and selectivity in ethanol sensing. The primary significance of this work lies in leveraging the unique capabilities of CBD to create a high-performance ethanol sensor. We delve deeply into the underlying mechanisms governing both electron and chemical sensitization pathways, ultimately elucidating the origins of oxygen vacancies within the material. This research holds the potential to bridge critical gaps in the development of CBD-based gas sensors, ultimately advancing the state of the art in this field and opening exciting new avenues for environmental monitoring and industrial safety applications.

Experimental section

Device fabrication

The ethanol vapor sensor, based on Pd/In_2O_3 hybrid NCs, was fabricated by depositing NCs onto a silicon oxide substrate with prefabricated IDEs, following a procedure similar to our previous report.[33,40,41] In contrast to prior research efforts, a dual-magnetron sputtering gun (gas aggregation cluster source) was integrated into a custom-made gas-phase cluster beam deposition system (CBDS) to sequentially deposit In and Pd NCs onto the substrate, as illustrated in Scheme 1.

Indium NCs were generated through sputtering of a high purity In target at 7 W using a direct current power supply (Advanced Energy, MDX-500 dual) under a 100 Pa argon (Ar, with purity higher than 99.999%, purchased from Hangzhou

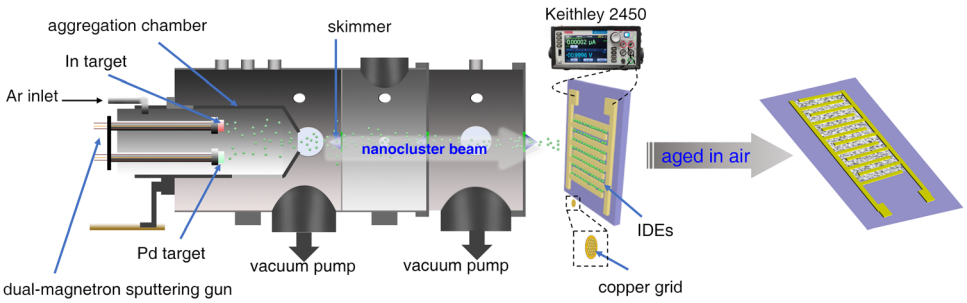

Scheme 1 Schematic diagram of the fabrication of the ethanol vapor sensor device based on Pd/In_2O_3 hybrid NCs.

Jingong Special Gas Co., Ltd) environment. This established an Ar atmosphere with a flow rate of 130 sccm, controlled by a mass flow controller (MFC, Aitoly, MFC300). A quartz microbalance (Sciens, SI-TM106) monitored the deposition rate of NCs onto a substrate (not depicted in Scheme 1). A differential pumping system subsequently transported the formed In NCs to a high-vacuum deposition chamber (not depicted) at a rate of 0.8 Å s^{-1}. During this process, a computer-controlled sourcemeter (Keithley 2450) continuously monitored the current across the IDEs under a 1.0 V bias voltage. Once a predetermined current value was reached, the sputtering process was terminated, signifying the completion of In NCs deposition. Following the same parameters, a subsequent deposition of Pd NCs onto the substrate was performed. The In and Pd targets used in the experiment were purchased from Beijing Zhongcheng New Materials Technology Co., Ltd, with purity higher than 99.99%. Following deposition, the samples underwent natural oxidation in air at room temperature for 12 days.

Characterization and measurements

The morphology and structure of the Pd/In_2O_3 hybrid NCs were characterized using transmission electron microscopy (TEM, Tecnai G2 F30 S-Twin, 300 kV) equipped with energy-dispersive spectroscopy (EDS). For TEM analysis, even in the high-resolution mode (HRTEM), Pd/In_2O_3 NCs were deposited on amorphous carbon films supported by copper grids positioned near the IDEs during sensor fabrication (Scheme 1). X-ray photoelectron spectroscopy (XPS, Kratos AXIS Ultra DLD) was used to analyze the electronic properties and chemical states of the Pd/In_2O_3 hybrid NCs. XPS binding energies were calibrated using the C 1s peak (284.8 eV) for charge correction.

Scheme 2 depicts a schematic diagram of the gas-sensing performance testing system. Fabricated sensors were integrated into a custom-designed testing chamber equipped with a computer-controlled sourcemeter (Keithley 2450) for response signal measurement. The chamber features a temperature-controlled sample stage, maintained using a PID (proportional integral derivative) controller. Target gases for testing were generated *via* the bubble method.[42–44] Briefly, ethanol vapor and other volatile organic compounds (VOCs) like acetone, toluene, and benzene were prepared at varying concentrations by bubbling dry air through pure liquid solutions. Mass flow controllers (MFCs, Aitoly MFC300, MKS 1179A) adjusted the gas concentrations by regulating the flow ratio of background gas and bubbling gas. For ethanol vapor sensing under different relative humidity (RH) conditions, dry air was replaced with saturated water vapor generated similarly, bubbling through solutions of K_2CO_3, NaBr, and KNO_3 to achieve 40%, 60%, and 90% RH, respectively.

In the process of characterizing the gas-sensing behaviors, the sensing signals were acquired by loading a 1 V DC voltage on the sample while measuring the current of the sample. Consistent with our previous publications,[39,45] the response of the sensor is defined as $R = \Delta I/I_a$, where $\Delta I = I_g - I_a$; I_g and I_a represent the current values under target gas and baseline (no target gas) conditions, respectively. Response and recovery times were determined as the time taken for the current to reach 90% of the saturated response upon exposure to the target gas and to decrease by 90% back to baseline after removal, respectively.

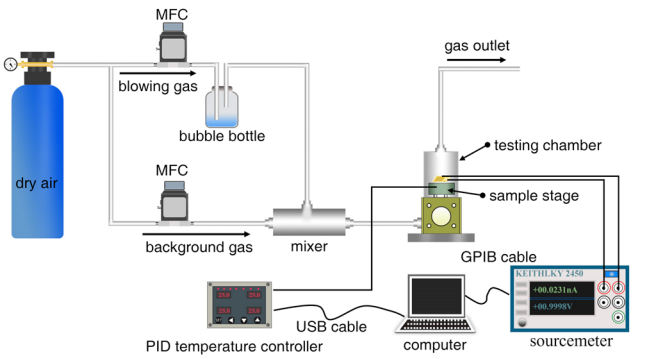

Scheme 2 Schematic diagram of the gas-sensing measurement system.

Results and discussion

A characteristic feature of current evolution during the deposition of In and Pd NCs is illustrated in Fig. 1a as a function of deposition time. Notably, during the deposition of In NCs, a discernible increase in the current across the IDEs was observed starting at approximately 700 seconds. As the deposition progressed until 1750 seconds, the In NCs deposition was halted, and the current stabilized at a relatively constant value of 20 nA. Subsequently, around 1880 seconds, the deposition of Pd NCs commenced, leading to a further and significant increase in the current, indicative of the Pd NCs acting as a bridging percolation pathway. Then, at approximately 2100 seconds, the deposition of Pd NCs was terminated, resulting in the current reaching 35 nA.

Following this, the Pd/In hybrid NCs were aged in an ambient environment for a minimum of 12 days to allow for the complete formation of indium oxide. As depicted in Fig. 1b, a sharp decrease in current was observed during the initial six days, followed by a plateau. This behavior is attributed to the oxidation of In NCs, suggesting that a minimum aging period of six days is necessary to ensure thorough oxidation.

Fig. 1c presents the TEM image of the sample obtained as described above, wherein the NCs exhibit a disorderly arrangement. The TEM image reveals significant contrasts between In_2O_3 and Pd NCs; the lighter regions are In_2O_3 NCs, and the darker regions are Pd NCs. This contrast is attributed to their distinct electron scattering and varying atomic numbers. Employing this effective distinction between In_2O_3 and Pd, the statistical analysis of the sizes (the inset in Fig. 1c) demonstrates a log-normal size distribution with an average size of 4.6 nm. Such a small size corresponds to an approximately estimated surface-to-volume ratio of 1.3×10^9 m^{-1}, which facilitates the realization of high-performance gas-sensing.

Fig. 1d displays the HRTEM image. The lattice spacing of Pd/In_2O_3 was calculated using Fourier inversion and determined

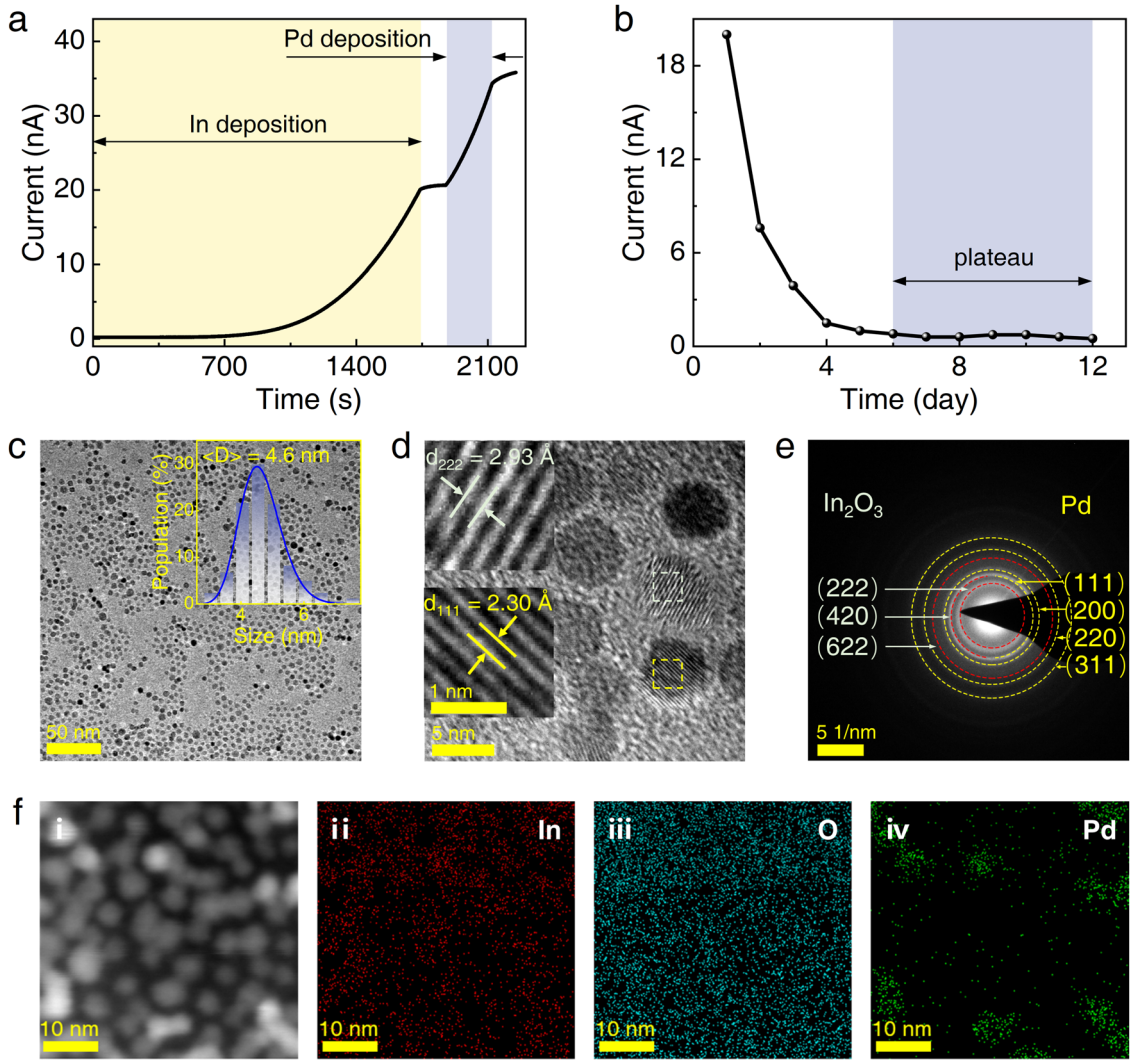

Fig. 1 Current evolution through sensor device during deposition and aging, and the corresponding TEM images. (a) Current across the IDEs as a function of deposition time. (b) The evolution of electric current passing through the IEDs of the sensor device during the aging process. (c) TEM image and size distribution of Pd/In_2O_3 hybrid NCs, where the blue line is a log-normal fitting. (d) HRTEM image of Pd/In_2O_3 NCs, with a magnified view of the region of interest (inset). (e) SAED pattern. (f) EDS mapping of Pd/In_2O_3: (i) TEM images of elements distributed over (ii) In, (iii) O, and (iv) Pd.

to be 0.230 nm, which corresponds to the (111) crystal plane of Pd (PDF# 00-001-1310), and 0.293 nm, which corresponds to the (222) crystal plane of In_2O_3 (PDF# 00-006-0416). The selected area electron diffraction (SAED) spectrum of Pd/In_2O_3 in Fig. 1e illustrates the polycrystalline structure, with lattice spacing attributed to Pd (PDF# 00-001-1310) for (111), (200), (220), (311),[46] and (331) crystal planes, and (222), (420), and (622) crystal planes corresponding to In_2O_3 (PDF# 00-006-0416).[47,48] The EDS mapping results depicted in Fig. 1f confirm the presence of In, O, and Pd elements distributed throughout the entire NCs.

To delve deeper into the chemical states of the elements, XPS measurements were conducted. In the In 3d spectrum, depicted in Fig. 2a, the peaks of In_2O_3 at 451.7 and 444.1 eV correspond to In^{3+} $3d_{3/2}$ and In^{3+} $3d_{5/2}$,[49] respectively. It is worth noting that the In 3d peaks of Pd/In_2O_3, positioned at 452.2 and 444.7 eV, assigned to In^{3+} $3d_{3/2}$ and In^{3+} $3d_{5/2}$, slightly shift towards higher energy levels. The disparity in binding energies of In 3d between the two samples arises from electron transfer occurring between In_2O_3 and Pd at the interface, attributed to their distinct work functions.[41] In general, electron transfer induces an electron-depleted space charge region,[19] leading to an enhancement in gas-sensing performance. This suggests that the surface modification of In_2O_3 by Pd holds the potential to augment sensitivity to ethanol vapors.

Fig. 2b illustrates the O 1s spectral peaks, which can be categorized into two peaks for pure In_2O_3 and three peaks for O 1s in Pd/In_2O_3. The peaks at 531.8 and 531.6 eV in both cases are attributed to lattice oxygen (O_L), while the peaks at 533.4 and 532.9 eV correspond to chemisorbed oxygen species (O_a). Notably, the peak at 535.1 eV, arising from oxygen vacancies (O_v), is exclusively observed in Pd/In_2O_3, with no presence of this peak in pristine In_2O_3. The content of these oxygen species can be obtained from the area of these peaks, as detailed in Table 1.

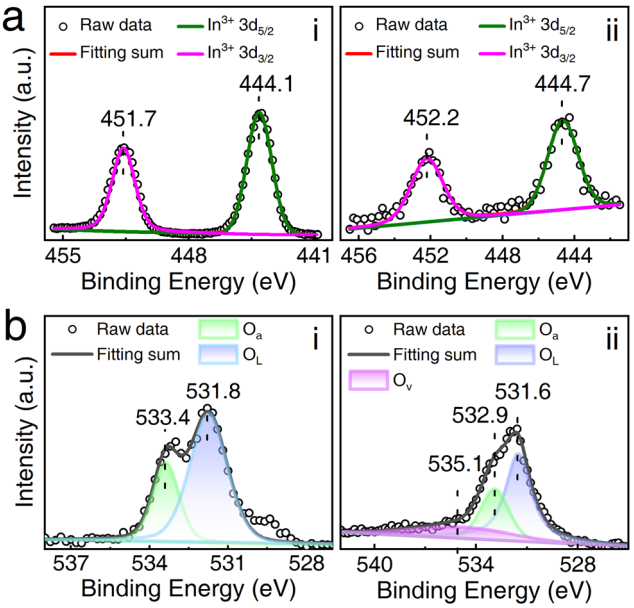

Fig. 2 Chemical state analysis. (a) In 3d XPS spectra of (i) In_2O_3 and (ii) Pd/In_2O_3. (b) O 1s XPS spectra of (i) In_2O_3 and (ii) Pd/In_2O_3.

Table 1 XPS analysis of O 1s of pure In_2O_3 and Pd/In_2O_3

Materials	O_L (%)	O_{ads} (%)	O_V (%)
In_2O_3	72.3	27.7	0
Pd/In_2O_3	54	26.4	19.6

It is evident that there is minimal difference in chemisorbed oxygen content between Pd/In_2O_3 and pristine In_2O_3. However, Pd/In_2O_3 exhibits a notable oxygen vacancy content of up to 19.6%, attributed to the introduction of Pd creating additional oxygen defects on the In_2O_3 surface. Oxygen vacancies on the surface of metal oxides have been identified as crucial factors in enhancing gas-sensing performance.[19,50] In this context, each oxygen vacancy provides one active center and releases electrons. The increased number of active centers facilitates the generation of more adsorbed oxygen species. Consequently, the augmentation of oxygen vacancies is anticipated to promote the adsorption of oxygen molecules on the sensitive material's surface, generating more active oxygen species and thereby favoring the acceleration of redox reactions on the sensitive material's surface.

Typically, the loading amount of noble metal significantly influences the gas-sensing properties of metal-oxide semiconductors.[51,52] Therefore, in our study, it is crucial to first elucidate the loading amount of Pd NCs on In_2O_3 NCs. Pristine In_2O_3 NCs and three samples with varying Pd loading amounts were prepared by adjusting the deposition time of Pd NCs. The Pd loading amounts for the three samples, determined through EDS spectral analysis (Fig. S1 in the ESI†), were calculated to be approximately 2, 6, and 12 atomic percent (at%) (denoted as *x* at% Pd/In_2O_3, where *x* represents the amount of Pd in atomic ratio).

The sensing response as a function of the operating temperature for pristine In_2O_3 and the three Pd/In_2O_3 samples, ranging from 150 to 280 °C, is summarized in Fig. 3a, with 100 ppm ethanol supplied. It is evident that all samples exhibited their highest sensing response to ethanol vapor at approximately 260 °C, which represents the optimal operating temperature for the device. Additionally, the 6 at% Pd/In_2O_3 demonstrated a higher response compared to the other samples, with a value reaching up to 101.2. This preliminary result indicates that the 6 at% Pd/In_2O_3 exhibits the highest sensitivity. The dynamic response of the four sensors to ethanol vapor at the optimum operating temperature is illustrated in Fig. 3b. The response of all sensors increases with the escalation of ethanol vapor concentration within the range of 50 to 1000 ppm.

Fig. 3c and d depict the linear relationship between the response of pristine In_2O_3 and the other three Pd/In_2O_3 samples *versus* the square root of ethanol vapor concentration, ranging from 50 to 1000 ppm, respectively. The response of pristine In_2O_3 saturates as the ethanol vapor concentration reaches 600 ppm or more. In contrast, the other sensors can effectively measure ethanol concentrations up to 1000 ppm. This extended detection range is primarily attributed to the generation of defective lattice oxygen in In_2O_3 induced by the loading of Pd NCs. This loading creates oxygen vacancies, providing more active sites for the adsorption of ethanol. Consequently, it expands the detection range, allowing the sensors to function optimally at higher ethanol concentrations.

According to the international union of pure and applied chemistry (IUPAC) definition,[53] the slope of the calibration curve serves as a representative measure of the sensor's sensitivity. We acknowledge the importance of further attention to the sensitivity value of our sensor. Here, in light of the observed linear relationship between sensor response and the square root of ethanol vapor concentration, we have utilized this relationship to construct a calibration curve to deduce the sensor's sensitivity. The sensitivity of pristine In_2O_3 is only 2.28 $ppm^{-1/2}$, while the 6 at% Pd/In_2O_3 exhibits the highest sensitivity of 28.24 $ppm^{-1/2}$. This observation indicates that the loading of Pd significantly enhances the sensitivity, and there exists an optimal Pd loading value, emphasizing that a higher loading is not necessarily better. This implies that an excessive amount of Pd loading may not lead to a proportionate increase in the sensor's response. Two primary reasons account for this: first, an excessive Pd loading may result in the agglomeration of NCs (see Fig. S1 in the ESI†), thereby reducing the total specific surface area and diminishing the adsorption of oxygen. Second, an excessive Pd presence may occupy some of the reactive active sites, consequently diminishing the sensor's response value.

The response and recovery times were measured for the pristine In_2O_3 and 6 at% Pd/In_2O_3 at 100 ppm ethanol, as depicted in Fig. 3e and f. The response and recovery times were 3.1 and 14.1 seconds, as well as 2.7 and 4.4 seconds for the pristine In_2O_3 and 6 at% Pd/In_2O_3, respectively. This outcome indicates that the loading of Pd primarily shortens the response time of the sensor while having little effect on the recovery time. Theoretically, the recovery time of metal oxide semiconductor-based sensors is predominantly influenced by two factors: the rate

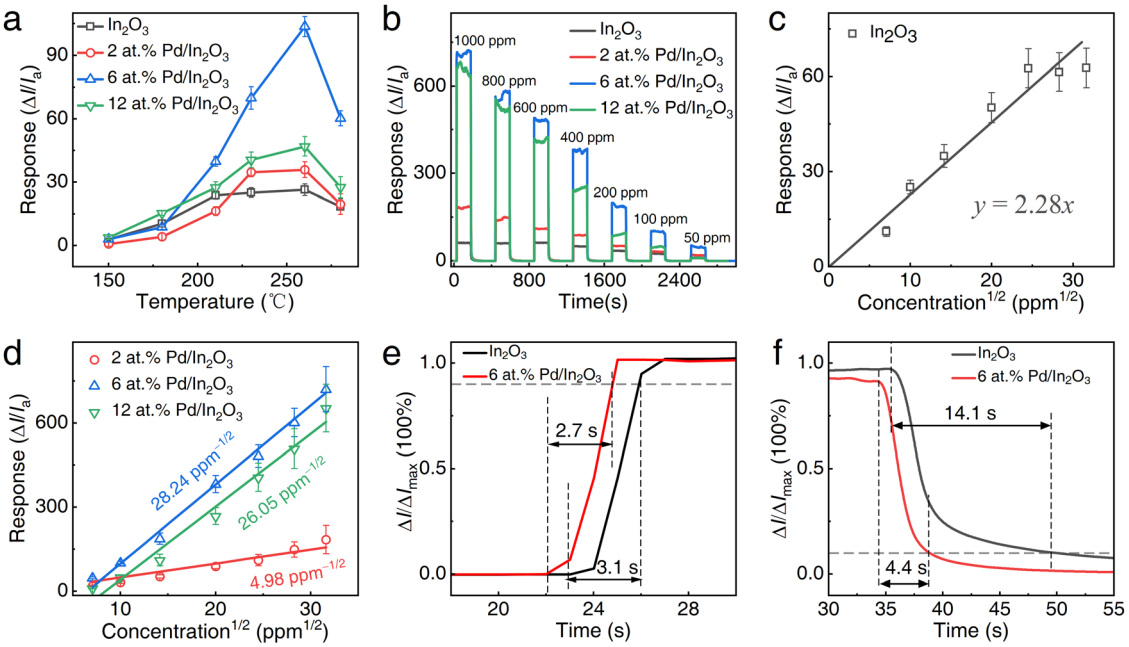

Fig. 3 Effect of the Pd loading amount on the gas-sensing performance. (a) Response values of pristine In_2O_3 and the three samples with Pd loading amounts of 2, 6, and 12 at% to 100 ppm ethanol vapor as a function of operating temperature. (b) The dynamic responses of the four samples to ethanol vapor concentrations from 50 to 1000 ppm at the optimum operating temperature of 260 °C. The concentration (in ppm) for each ethanol vapor loading is marked at the top of each response peak. (c) and (d) The response *versus* square root of ethanol vapor concentration from 50 to 1000 ppm and fitted by a linear equation. The slopes of the linear fitting are indicated. (e) and (f) Normalized response and recovery signal $\Delta I/\Delta I_{max}$ of the 6 at% Pd/In_2O_3 toward 100 ppm ethanol vapor at 260 °C. The horizontal dashed lines indicate $\Delta I/\Delta I_{max}$ = 0.9, where ΔI_{max} is the maximum change in the response current.

of desorption of gas-sensing reaction products and the rate of regeneration of chemisorbed oxygen on the metal oxide semiconductor (MOS) surface. In this study, the faster recovery rate of the 6 at% Pd/In_2O_3 may imply that Pd NCs can not only expedite the regeneration of chemisorbed oxygen through its strong overflow effect but also catalyze the gas-sensing reaction, producing products that can be easily desorbed from the In_2O_3 surface.

In addition to evaluating sensitivity and sensing kinetics performance, the 6 at% Pd/In_2O_3 sensor was subjected to testing at the optimal operating temperature to further assess its qualitative performance, encompassing repeatability, moisture resistance, long-term stability, and selectivity. The repeatability of our device was evaluated by subjecting the 6 at% Pd/In_2O_3 sensor to 10 loading–unloading cycles of 100 ppm ethanol (Fig. 4a). The sensor demonstrated a consistent response of 100 ± 6 and consistently reverted to its original state after each cycle, highlighting its noteworthy repeatability and reversibility.

Fig. 4b illustrates the response of the 6 at% Pd/In_2O_3 sensor to 100 ppm ethanol at varying relative humidity (RH) levels. As RH increases from 25% to 90%, the response value decreases from 94.5 to about 70.5. This phenomenon is attributed to the adsorption of water molecules on the surface of Pd/In_2O_3 NCs, competing with ethanol molecules for reactions with chemisorbed oxygen. Despite this common issue with metal oxide semiconductors (MOS) as gas-sensing materials, our sensors exhibit reliable operation across a wide RH range, from 0 to 90%.

The selectivity of the 6 at% Pd/In_2O_3 sensor was investigated by comparing its responses to six widely used gases, namely acetone, toluene, benzene, ammonia, methanol, and isopropanol, each at a concentration of 100 ppm. As depicted in Fig. 4c, the responses of the 6 at% Pd/In_2O_3 sensor to these gases are lower than that observed for 100 ppm ethanol. Fig. 4d depicts the selectivity test for various volatile organic gases. It is evident that the sensor's response values for ethanol are considerably higher than those for the other six gases, confirming the sensor's notable selectivity for ethanol.

In this study, due to experimental constraints, ethanol vapor concentrations below 50 ppm were not investigated. Nonetheless, the limit of detection (LOD) of the sensor was determined using the 3σ method.[54] The LOD is defined as the concentration value corresponding to three times the baseline noise of the sensor (3σ). The baseline noise, represented by σ, was determined to be 0.00785 by analyzing the relative rate of change of the sensor baseline, as illustrated in Fig. 4e. While Fig. 3d illustrates a linear relationship between the sensor response and the square root of ethanol concentration across a wide concentration range, it is evident that the response demonstrates linearity with ethanol concentration over a narrower range, particularly below 100 ppm concentration, as shown in Fig. 4f. Leveraging this linear relationship and the standard deviation σ obtained in Fig. 4e, an LOD of 24 ppb was determined.

Fig. 4g presents a stability test of the 6 at% Pd/In_2O_3 sensor exposed to 100 ppm ethanol over 30 days. Results indicate a consistent sensor performance, with only a minor decrease in

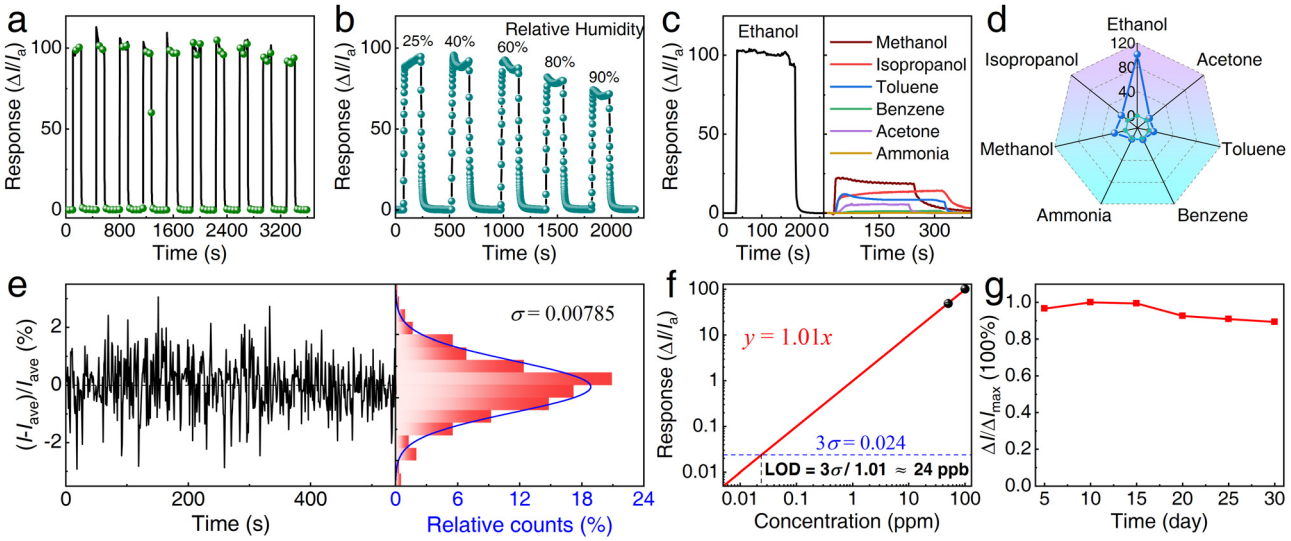

Fig. 4 Repeatability, impact of relative humidity (RH), stability, and selectivity of our ethanol vapor sensors. (a) Response curve of the 6 at% Pd/In_2O_3 sensor at 100 ppm ethanol at an operating temperature of 260 °C. (b) Response curve at different relative humidity levels. (c) Response curves for the 6 at% Pd/In_2O_3 sensor exposed to various volatile organic compounds (VOCs). (d) Measured sensor response to common VOCs, including acetone, toluene, benzene, ammonia, methanol, and isopropanol, compared with the sensor response to 100 ppm ethanol. (e) Statistical analysis of noise observed for the 6 at% Pd/In_2O_3 at 260 °C, averaging the current signal (I_{ave}) of the sensor for 550 s when the sensor was in air. The noise distribution exhibits a normal distribution with standard deviation σ = 0.00785. (f) log–log graph of the relationship between sensor response and ethanol concentration within the range of less than 100 ppm. The response amplitude was extracted from the sensing signal at 50 and 100 ppm, shown in Fig. 3b. (g) Change in normalized response along time elapses within 30 days.

response observed over the 30-day period. A maximum decline of merely 9% in the response underscores the sensor's high stability, durability, and repeatability without significant performance degradation.

A comparative analysis of ethanol vapor sensing properties between literature-reported In_2O_3 and the 6 at% Pd/In_2O_3 employed in this study is presented in Table 2. To the best of our knowledge, our sensor epitomizes the current state of the art in optimized comprehensive sensing capabilities, encompassing response and recovery time, sensitivity, and manufacturing technology. Therefore, Pd/In_2O_3 hybrid NCs emerge as a promising material for ethanol gas sensors.

Investigating the sensing mechanism, electron sensitization, and chemical sensitization are recognized as predominant mechanisms contributing to the enhancement of gas-sensing properties through noble metal decoration.[63] However, within the scope of this study, the following question arises: which mechanism predominantly governs the enhancement of gas-sensing properties?

The underlying sensing mechanism of chemiresistive MOS-based gas sensors is rooted in the oxygen adsorption model.[19] In ambient air, oxygen molecules accumulate on the MOS surface, forming chemisorbed oxygen species (O_2^-, O^-, or O^{2-}) by capturing electrons. The reaction processes are listed as follows:

$$O_2(gas) \rightarrow O_2(ads) \quad (1)$$

$$O_2(gas) + e^- \rightarrow O_2^-(ads) \quad (2)$$

Table 2 Comparison of the sensing performance of various ethanol vapor sensing materials

Materials	Ethanol concentration (ppm)	Response amplitude	Apparent sensitivity[a] (ppm^{-1})	Response time (s)	Recovery time (s)	Operating temperature (°C)	Ref.
Pb-doped In_2O_3	100	32.57	0.33	2.2	0.7	250	55
Sn-doped In_2O_3	100	8	0.08	9	3.9	330	56
Dy^{3+}-doped In_2O_3	50	55	1.1	12	36	300	57
In_2O_3@MoS_2	100	51	0.51	8	20	260	58
Ho-doped In_2O_3	100	60	0.6	4	28	240	59
Au-doped In_2O_3	100	16.16	0.16	5	64	160	60
Pd-doped In_2O_3	100	39	0.39	25	9	250	61
Eu_2O_3–In_2O_3	50	44	0.88	3	21	260	62
In_2O_3 NCs	100	25.2	0.25	3.1	14.1	260	This work
Pd/In_2O_3 hybrid NCs	100	101.2	1.01	2.7	4.4	260	This work

[a] In some of the references cited in Table 2, the relationship between sensor response and ethanol vapor concentration is not strictly linear. To facilitate comparison, we have opted to present the ratio of sensor response to ethanol vapor concentration as apparent sensitivity.

$$O_2^-(ads) + e^- \rightarrow 2O^-(ads) \quad (3)$$

$$O^-(ads) + e^- \rightarrow O^{2-}(ads) \quad (4)$$

This process generates an electron depletion layer (for n-type MOS) or a hole accumulation layer (for p-type MOS), leading to increased or decreased resistance. The reaction involves adsorption and electron transfer, and when exposed to target gases, the adsorbed molecules react with chemisorbed oxygen, either releasing electrons (for reducing gases) or extracting more electrons (for oxidizing gases). This interaction modifies the width of the electron depletion layer/hole accumulation layer, altering MOS resistance and indicating sensor sensitivity.[19]

Noble metal decoration enhances gas-sensing through electronic sensitization and chemical sensitization.[63] In electronic sensitization, electrons transfer between noble metals and MOS, forming a Schottky barrier that increases the electron depletion layer's thickness, leading to a significant resistance change upon exposure to gases. Chemical sensitization involves noble metals facilitating the dissociation of oxygen molecules, producing reactive oxygen ions that react with target gas molecules, resulting in improved gas-sensing performance. Additionally, noble metal decoration increases the specific surface area, providing more catalytic active sites for gas adsorption.

In the electronic sensitization mechanism, electron transfer occurs due to the mismatch of work functions between the metal oxide semiconductor (MOS) and the noble metal, a common phenomenon in noble metal-loaded MOS systems. In our study, if electron sensitization is operational, electrons must be transferred from In_2O_3 to Pd. Analyzing the slight increase in the binding energy of In 3d in Pd/In_2O_3 compared to pristine In_2O_3 (Fig. 2a) and the decrease in the binding energy of Pd in Pd/In_2O_3 relative to pure Pd (Fig. S2, ESI†), we can confidently assert that electrons are indeed transferred from In_2O_3 to Pd. Therefore, we can reasonably conclude that the electronic sensitization mechanism plays a significant role in our devices.

In the chemical sensitization process, noble metals play a crucial role in facilitating the dissociation of oxygen molecules, giving rise to additional reactive chemisorbed oxygen ions. These ions subsequently spill over onto the surface of the MOS and interact with a greater number of target gas molecules. This phenomenon, commonly referred to as the spillover effect, underscores the heightened reactivity achieved through chemical sensitization. As illustrated in Fig. 3f, the response time of Pd/In_2O_3 is significantly reduced compared to pristine In_2O_3. During the recovery phase of the gas sensor, oxygen is re-adsorbed onto the MOS surface. This process extracts electrons from the conduction band and traps them at the surface as ions, leading to band bending. The result is the reformation of the electron depletion layer, causing an increase in the resistance of the MOS. This gradually restores it to near its initial level. Therefore, the recovery time is predominantly determined by the rate of oxygen re-adsorption on the MOS surface. The markedly reduced response time in Pd/In_2O_3 can be attributed to the catalytic effect of Pd, suggesting that the chemical sensitization mechanism also plays a crucial role. In addition, the modification with Pd led to a significant increase in the number of oxygen vacancies (Fig. 2b). This increase would enhance the amount of adsorbed oxygen on the surface, consequently inducing a further enhancement in sensitivity.

Based on the preceding analysis, the enhanced performance of Pd/In_2O_3 hybrid NC-based gas sensors can be attributed to the synergistic effects of electronic sensitization, chemical sensitization, and increased oxygen vacancies. This collaborative interplay contributes to heightened sensitivity, improved sensing kinetics, and underscores the diverse advantages of noble metal decoration in optimizing MOS-based gas sensors.

Conclusions

In summary, we have developed a highly sensitive and selective ethanol sensor utilizing palladium-decorated indium trioxide (Pd/In_2O_3) nanoclusters (NCs) synthesized *via* cluster beam deposition (CBD). The sensor demonstrated exceptional performance, with a notable sensitivity of 28.24 $ppm^{-1/2}$ and rapid response and recovery times of 2.7 and 4.4 seconds, respectively. The LOD is as low as 24 ppb. The optimal sensor performance was achieved with a Pd loading of 6 at%, highlighting the critical role of Pd in enhancing the sensor's sensitivity and response times. The enhanced performance of the Pd/In_2O_3 hybrid NC-based gas sensors can be attributed to the synergistic effects of electronic sensitization, chemical sensitization, and significant oxygen vacancies. The electronic sensitization mechanism, facilitated by the transfer of electrons from In_2O_3 to Pd, played a significant role in our devices. Additionally, the chemical sensitization process, characterized by the spillover effect, contributed to the heightened reactivity and reduced response and recovery times of the sensor. The modification with Pd also led to a significant increase in the number of oxygen vacancies, further enhancing the sensor's sensitivity. This study emphasizes the potential of Pd/In_2O_3 hybrid NCs as a promising material for ethanol vapor detection and underscores the advantages of employing CBD in synthesizing noble metal-loaded MOS nanomaterials. The research contributes to the advancement of gas-sensing technology and opens new avenues for the development of sensitive and selective ethanol sensors for environmental monitoring and industrial safety applications.

Author contributions

Bo Xie and Peng Mao conceived the project, collected and analyzed the data, and wrote the manuscript mainly. Jian Sun carried out all the experiments and wrote the manuscript partly. Aoxue Zhang, Haoyu Qian, Xibing Mao, Yingzhu Li, and Wenjing Yan provided support for the experiments related to the device and materials characterization. Changjiang Zhou, Hui-Min Wen, and Shengjie Xia helped with experiments related to sensing and analysis. Paolo Milani participated in

discussing the data. Min Han and Peng Mao supervised the project.

Conflicts of interest

There are no conflicts to declare.

Acknowledgements

This work was supported by the National Natural Science Foundation of China (Grant no. 12374256, 92061126, 22278371, 92163110, 12274213, 12104220) and the Open Foundation of the State Key Laboratory of Fluid Power and Mechatronic Systems (Grant no. GZKF-202217).

References

1 W. Yan, Y. Chen, X. Zeng, G. Wu, W. Jiang, D. Wei, M. Ling, K. Wei Ng and Y. Qin, *Appl. Surf. Sci.*, 2021, **535**, 147697.
2 B. Jiang, J. Lu, W. Han, Y. Sun, Y. Wang, P. Cheng, H. Zhang, C. Wang and G. Lu, *Sens. Actuators, B*, 2022, **357**, 131333.
3 Q. Wang, J. Hong, Z. Zhang, J. Li, X. Cao, J. Tang, Y. Geng, J. Wang, X. Li, K. Pei, Y. Du and X. Tian, *Sens. Actuators, B*, 2022, **370**, 132399.
4 X. Wang, J. Gao, Z. Chen, H. Chen, Y. Zhao, Y. Huang and Z. Chen, *Renewable Energy*, 2022, **194**, 504–525.
5 P. Snitkjær, J. Ryapushkina, E. Skovenborg, A. Astrup, L. M. Bech, M. G. Jensen and J. Risbo, *Food Chem.*, 2017, **230**, 234–240.
6 A. Mirzaei, S. G. Leonardi and G. Neri, *Ceram. Int.*, 2016, **42**, 15119–15141.
7 Z. Wang, Z. Tian, D. Han and F. Gu, *ACS Appl. Mater. Interfaces*, 2016, **8**, 5466–5474.
8 W. Wang, S. Kang, W. Zhou and P. J. Vikesland, *Environ. Sci.: Nano*, 2023, **10**, 393–423.
9 R. Pal, K.-H. Kim, Y.-J. Hong and E.-C. Jeon, *J. Hazard. Mater.*, 2008, **153**, 1122–1135.
10 Y. Zhao and J. Li, *Environ. Sci. Technol.*, 2022, **56**, 17531–17544.
11 J. Erfkamp, M. Guenther and G. Gerlach, *Sensors*, 2019, **19**, 1199.
12 S. Mu, W. Ren, M. Xu, P. He, D. Jia and C. Liu, *Sens. Actuators, B*, 2023, **384**, 133649.
13 B. Li, J. Liu, Q. Liu, R. Chen, H. Zhang, J. Yu, D. Song, J. Li, M. Zhang and J. Wang, *Appl. Surf. Sci.*, 2019, **475**, 700–709.
14 A. Dey, *J. Mater. Sci. Eng. B*, 2018, **229**, 206–217.
15 C. L. Lu, S. J. Chang, T. C. Weng and T. J. Hsueh, *IEEE Electron Device Lett.*, 2018, **39**, 1223–1225.
16 P. K. Shihabudeen and A. Roy Chaudhuri, *Sens. Actuators, B*, 2020, **305**, 127523.
17 L. Xiao, G. Li, Z. Yang, K. Chen, R. Zhou, H. Liao, Q. Xu and J. Xu, *Adv. Funct. Mater.*, 2021, **31**, 2100982.
18 Y. Chen, X. Zhang, Z. Liu, Z. Zeng, H. Zhao, X. Wang and J. Xu, *Microchim. Acta*, 2019, **186**, 47.
19 D. Degler, U. Weimar and N. Barsan, *ACS Sens.*, 2019, **4**, 2228–2249.
20 N. Sui, X. Wei, S. Cao, P. Zhang, T. Zhou and T. Zhang, *ACS Sens.*, 2022, **7**, 2178–2187.
21 W. Liu, J. Sun, L. Xu, S. Zhu, X. Zhou, S. Yang, B. Dong, X. Bai, G. Lu and H. Song, *Nanoscale Horiz.*, 2019, **4**, 1361–1371.
22 Y. Shen, X. Yan, S. Zhao, X. Chen, D. Wei, S. Gao, C. Han and D. Meng, *Sens. Actuators, B*, 2016, **230**, 667–672.
23 C. Zhang, Y. Huan, Y. Li, Y. Luo and M. Debliquy, *J. Adv. Ceram.*, 2022, **11**, 379–391.
24 P. Rai, J.-W. Yoon, C.-H. Kwak and J.-H. Lee, *J. Mater. Chem. A*, 2016, **4**, 264–269.
25 P. Cheng, Y. Wang, C. Wang, J. Ma, L. Xu, C. Lv and Y. Sun, *Nanotechnology*, 2021, **32**, 305503.
26 P. Mao, A. K. Mahapatra, J. Chen, M. Chen, G. Wang and M. Han, *ACS Appl. Mater. Interfaces*, 2015, **7**, 19179–19188.
27 P. Mao, C. Liu, G. Favraud, Q. Chen, M. Han, A. Fratalocchi and S. Zhang, *Nat. Commun.*, 2018, **9**, 5428.
28 C.-C. Hou, H.-F. Wang, C. Li and Q. Xu, *Energy Environ. Sci.*, 2020, **13**, 1658–1693.
29 P. Mao, C. Liu, F. Song, M. Han, S. A. Maier and S. Zhang, *Nat. Commun.*, 2020, **11**, 1538.
30 P. Mao, C. Liu, Y. Niu, Y. Qin, F. Song, M. Han, R. E. Palmer, S. A. Maier and S. Zhang, *Adv. Mater.*, 2021, **33**, 2007623.
31 P. Milani and S. Iannotta, *Cluster beam synthesis of nanostructured materials*, Springer Science & Business Media, 2012.
32 M. Chen, W. Luo, Z. Xu, X. Zhang, B. Xie, G. Wang and M. Han, *Nat. Commun.*, 2019, **10**, 4024.
33 B. Xie, P. Mao, M. Chen, Z. Li, J. Han, L. Yang, X. Wang, M. Han, J.-M. Liu and G. Wang, *ACS Appl. Mater. Interfaces*, 2018, **10**, 44603–44613.
34 R. E. Palmer, R. Cai and J. Vernieres, *Acc. Chem. Res.*, 2018, **51**, 2296–2304.
35 S. Mondal and D. Chowdhury, *Surf. Coat. Technol.*, 2020, **393**, 125776.
36 M. Bruzzi, S. Miglio, M. Scaringella, G. Bongiorno, P. Piseri and P. Milani, *Sens. Actuators, B*, 2004, **100**, 173–176.
37 P. Barman, A. Deka, S. Chakraborty and S. Bhattacharyya, *J. Phys. Chem. C*, 2021, **125**, 24576–24588.
38 C. Xirouchaki and R. Palmer, *Philos. Trans. R. Soc., A*, 2004, **362**, 117–124.
39 Y. Liu, Y. Lei, X. Mao, H. Qian, H.-M. Wen, S. Xia, Y. Xiang, Q. Chen, B. Xie and J. Hu, *Int. J. Hydrogen Energy*, 2024, **62**, 783–793.
40 B. Xie, H. You, H. Qian, S. Hao, Z. Li, Y. Qin, H.-M. Wen, S. Xia, Y. Xiang and J. Hu, *ACS Appl. Nano Mater.*, 2023, **6**, 7011–7021.
41 B. Xie, B. Ding, P. Mao, Y. Wang, Y. Liu, M. Chen, C. Zhou, H.-M. Wen, S. Xia, M. Han, R. E. Palmer, G. Wang and J. Hu, *Small*, 2022, **18**, 2200634.
42 N. D. Chinh, N. M. Hung, S. Majumder, C. Kim and D. Kim, *Sens. Actuators, B*, 2021, **326**, 128956.
43 G. W. Thomson, *Chem. Rev.*, 1946, **38**, 1–39.
44 Y.-C. Liang and T.-Y. Lin, *Nanoscale Res. Lett.*, 2014, **9**, 1–7.

45 H. Qian, A. Zhang, J. Sun, X. Mao, Y. Liu, H.-M. Wen, S. Xia, B. Xie and J. Hu, *Appl. Surf. Sci.*, 2024, **657**, 159735.
46 Z. Sun, X. Yan, L. Huang, Y. Zhang, Z. Hu, C. Sun, X. Yang, G. Pan and Y. Cheng, *Sens. Actuators, B*, 2023, **381**, 133355.
47 Y. Wang, X. Sun and J. Cao, *J. Alloys Compd.*, 2022, **895**, 162557.
48 Z.-H. Ma, R.-T. Yu and J.-M. Song, *Sens. Actuators, B*, 2020, **305**, 127377.
49 K. Zhang, Y. Shen, Z. Lin and Z. Dong, *Mater. Sci. Semicond. Process.*, 2021, **135**, 106124.
50 Y. Ou, G. Zhu, P. Liu, Y. Jia, L. Zhu, J. Nie, S. Zhang, W. Zhang, J. Gao, H. Lu, Y. Huang, X. Shi and M. Hojamberdiev, *ACS Sens.*, 2022, **7**, 1201–1212.
51 S.-Y. Jeong, J.-S. Kim and J.-H. Lee, *Adv. Mater.*, 2020, **32**, 2002075.
52 T. Zhou, Z. Qin, X. Wang, C. Wu, X. Tang, T. Zhang, H. Wang, C. Xie and D. Zeng, *Chem. Commun.*, 2019, **55**, 11045–11048.
53 L. A. Currie, *Pure Appl. Chem.*, 1995, **67**, 1699–1723.
54 G. L. Long and J. D. Winefordner, *Anal. Chem.*, 1983, **55**, 712A–724A.
55 A. Montazeri and F. Jamali-Sheini, *Sens. Actuators, B*, 2017, **242**, 778–791.
56 N. Jamalpoor, M. Ghasemi and V. Soleimanian, *Mater. Res. Bull.*, 2018, **106**, 49–56.
57 K. Anand, J. Kaur, R. C. Singh and R. Thangaraj, *Chem. Phys. Lett.*, 2017, **670**, 37–45.
58 X. Liu, L. Jiang, X. Jiang, X. Tian, Y. Huang, P. Hou, S. Zhang and X. Xu, *Appl. Surf. Sci.*, 2018, **447**, 49–56.
59 H. Duan, Y. Wang, S. Li, H. Li, L. Liu, L. Du and Y. Cheng, *J. Mater. Sci.*, 2018, **53**, 3267–3279.
60 J. Bai, Q. Wang, Y. Wang, X. Cheng, Z. Yang, X. Gu, B. Huang, G. Sun, Z. Zhang and X. Pan, *J. Colloid Interface Sci.*, 2020, **560**, 447–457.
61 P. Rai, J.-W. Yoon, C.-H. Kwak and J.-H. Lee, *J. Mater. Chem. A*, 2016, **4**, 264–269.
62 H. Lian, Y. Feng, Z. Wang, L. Liu, X. Guo and X. Wang, *Appl. Phys. A*, 2017, **123**, 1–6.
63 L.-Y. Zhu, L.-X. Ou, L.-W. Mao, X.-Y. Wu, Y.-P. Liu and H.-L. Lu, *Nano-Micro Lett.*, 2023, **15**, 89.